Continued increase in atmospheric CO_2 seasonal amplitude in the 21st century projected by the CMIP5 Earth system models

F. Zhao[1] and N. Zeng[1,2]

[1]{Department of Atmospheric and Oceanic Science, University of Maryland, USA}

[2]{Earth System Science Interdisciplinary Center University of Maryland, USA}

Correspondence to: N. Zeng (zeng@atmos.umd.edu)

Abstract

In the Northern Hemisphere, atmospheric CO_2 concentration declines in spring and summer, and rises in fall and winter. Ground-based and aircraft-based observation records indicate that the amplitude of this seasonal cycle has increased in the past. Will this trend continue in the future? In this paper, we analyzed simulations for historical (1850-2005) and future (RCP8.5, 2006-2100) periods produced by 10 Earth System Models participating the Fifth Phase of the Coupled Model Intercomparison Project (CMIP5). Our results present a model consensus that the increase of CO_2 seasonal amplitude continues throughout the 21st century. Multi-model ensemble relative amplitude of detrended global mean CO_2 seasonal cycle increases by 62±19% in 2981-2090, relative to 1961-1970. This amplitude change corresponds to a 68±25% increase in Net Biosphere Production (NBP). We then show the increase of NBP amplitude mainly comes from enhanced ecosystem uptake during Northern Hemisphere growing season under future CO_2 and temperature conditions. Separate analyses on Net Primary Production (NPP) and respiration reveal that enhanced ecosystem carbon uptake contributes about 75% of the amplitude increase. Stimulated by higher CO_2 concentration and high-latitude warming, enhanced NPP likely outcompetes increased respiration at higher temperature, resulting in a higher net uptake during the Northern growing season. Zonal distribution and the spatial pattern of NBP change suggest that regions north of 45°N dominate the amplitude increase. Models that simulate a stronger carbon uptake also tend to show a larger change of NBP seasonal amplitude, and the cross-model correlation is significant ($R=0.73$, $p<0.05$).

1 Introduction

Modern measurements at Mauna Loa, Hawaii (19.5°N, 155.6°W, 3400m altitude) has recorded the atmospheric CO_2 concentration increase from below 320 ppm in 1958 to over 400 ppm today. This CO_2 time series is also characterized by a mean seasonal cycle that comprises a 5-month decrease (minimum in October) and a 7-month increase (maximum in May). The peak-to-trough amplitude of this seasonal cycle is about 6.5 ppm, which has been shown to represent a close average of a large portion of the Northern Hemisphere biosphere (Kaminski et al., 1996), where the amplitude ranges from 3 ppm at 10°N to 17 ppm at Point Barrow, Alaska (71°N). The seasonal variation of Mauna Loa (MLO) CO_2 reflects the imbalance of growth and decay of the Northern Hemisphere biosphere. Early studies has speculated that global primary production would decrease because of global changes such as acid rain and cutting forest (Whittaker and Likens, 1973; Reiners 1973), in which case we might observe a reduction of CO_2 seasonal amplitude (assuming changes in respiration are similar at the peak and trough of the CO_2 seasonal cycle). However, Hall et al. (1975) found no evidence of a long-term change in amplitude from 15 years of MLO CO_2 record (1958-1972). They concluded either the biosphere is too big to be affected yet or the degradation of biosphere is balanced by enhanced CO_2 fertilization and increased use of fertilizers in agriculture.

As the industrialization processes expanded during the 1970s and 1980s, it seems likely that the metabolic activity of the biosphere became stronger, as indicated by a rapid increase in CO_2 seasonal amplitude computed from MLO CO_2 record (Pearman and Hyson, 1981; Cleveland et al., 1983; Bacastow et al., 1985). Enhanced CO_2 fertilization was considered as an obvious factor, and a change to climatic conditions a possible cause (Bacastow et al., 1985). Keeling et al. (1996) further linked the amplitude increase with climate change by showing the two-year phase lag relationship between trends in the relative amplitude and trends in 30-80°N mean temperature. They suggest the warming may also lead to a lengthening of growing season associated with phase advances of about 7 days during the declining phase of the seasonal cycle.

Unlike CO_2 fertilization, the combined effect of climate (temperature, precipitation, etc.) introduces strong interannual variability to the amplitude change, and changes in climate could either lead to an amplitude increase or decrease—it was noticed later that despite of the continuing rise of 30-80°N mean land temperature since 1990s, CO_2 seasonal amplitude at

MLO has declined. Buermann et al. (2007) attributed the decline to the severe drought in North America during 1998-2003. They reasoned that MLO receives mainly Eurasian air masses in the Northern Hemisphere winter but relatively more North American air masses in summer.

After the mid-1990s, the increasing trend of CO_2 seasonal amplitude resumed at MLO. The latest analysis shows a 0.32% yr^{-1} increase in MLO amplitude and a 0.60% yr^{-1} increase in Point Barrow (Figure 1A, Graven et al., 2013). Over a 50-year period, this corresponds to an increase of 16% and 30% in MLO and Point Barrow CO_2 seasonal amplitude, respectively. Graven et al. (2013) also compared aircraft measurements taken at 500hPa and 700hPa heights in 1958–1961 and 2009–2011, and these data suggest an even larger (~50%) increase of atmospheric CO_2 seasonal amplitude north of 45°N. Then they applied two atmospheric transport models to monthly Net Ecosystem Production (NEP) from the historical simulation (Exp3.2) results of eight Coupled Model Intercomparison Project Phase 5 (CMIP5) models, in order to infer the model-simulated CO_2 amplitude increase at 500hPa. Compared with aircraft data, they found the CMIP5 models simulated a much lower amplitude increase.

So far, the magnitude of global mean CO_2 amplitude change is not clear. Even though the Global Monitoring Division of NOAA/Earth System Research Laboratory (ESRL) has measured carbon dioxide for several decades at well over 100 surface CO_2 monitoring sites (Conway et al., 1994), fewer than 20 of them have over 30 years of record. Randerson et al. (1997) analyzed flask data from some of the stations, and they found an amplitude trend of 0.66% yr^{-1} over five stations north of 55°N from 1981 to 1995. Interestingly, they also detected a higher increase (0.69% yr^{-1}) in flask measurements at Mauna Loa (1976-1995) than the trend (0.45% yr^{-1}) measured at Point Barrow (1971-1995). Perhaps one of the best global monthly mean CO_2 time series (since 1980) is provided by ESRL (Ed Dlugokencky and Pieter Tans, NOAA/ESRL, www.esrl.noaa.gov/gmd/ccgg/trends/), computed from 43 remote stations that sample well-mixed marine boundary layer (MBL). Another source of estimate is from atmospheric inversions, which give spatially explicit surface fluxes in addition to global mean. However, their resolution and accuracy are inherently limited due to a small number of stations used, and errors in atmospheric transport (Peylin et al., 2013).

Process-based Terrestrial Biosphere Models (TBMs) can generate surface fluxes over the past century or longer, usually with a spatial resolution of half to three degrees. They offer insights in better understanding the mechanisms for the amplitude change. McGuire et al. (2001) compared the relative change of the seasonal amplitude of total land-atmosphere carbon flux north of 30°N from four TBMs in comparison to Mauna Loa CO_2 observations, and they found the trend was overestimated by one of the four models and underestimated by the other three. They suggest the observed trend may be a consequence of the combined effects of rising CO_2, climate variability and land use changes, which has also been noted in previous studies(Kohlmaier et al., 1989; Keeling et al., 1995, 1996; Randerson et al., 1997, 1999; Zimov et al., 1999). Models show varied extent of amplitude increase, which is likely due to their different sensitivities to CO_2 concentration and climate. It is especially interesting that while Graven et al. (2013) found CMIP5 models underestimate the CO_2 amplitude change in the mid-troposphere at latitudes north of 45°N, previous observation indicated the models might overestimate CO_2 fertilization effect (Piao et al., 2013), suggesting that our understanding of the CO_2 seasonal amplitude problem is still limited.

With temperature rise and CO_2 increase, we may see further lengthening of growing season over high latitudes. On the other hand, the atmospheric circulation patterns will also change; the frequency and/or duration of heat waves are very likely to increase over most land areas, and the Increases in intensity and/or duration of drought and flood are likely (International Panel on Climate Change, 2013). It is not clear whether the net effect of natural and human-induced environmental changes would result in an increase or decrease of the amplitude in the future. In this study, we analyzed the fully coupled CMIP5 earth system model runs as part of the Fifth Assessment Report (AR5) of the United Nations' Intergovernmental Panel on Climate Change (IPCC). Specifically, we looked into the emission-driven simulations, which include many of the aforementioned processes and feedbacks. Our goal is to answer the following questions: How do CMIP5 models predict the amplitude and phase changes of CO_2 seasonal cycle in the future? Are the changes mostly driven by changes in production or respiration? Where do the models predict the largest amplitude changes will occur?

Section 2 describes the CMIP5 experiments, models used and our analyzing method; section 3 presents the major results of our multi-model analyses; sections 4 discuss and conclude our main findings.

2 Method

2.1 Model descriptions

We analyzed historical and future emission-driven simulation results from 10 CMIP5 ESMs. The historical simulations, referred to as experiment 5.2 or ESM historical 1850-2005 run (Taylor et al., 2012), were forced with gridded CO_2 emissions reconstructed from fossil fuel consumption estimates (Andres et al., 2011). Unlike the concentration-driven (no feedback on CO_2 concentration in the atmosphere) future simulations with four different Representative Concentration Pathways (RCPs), the emission-driven future simulations, referred to as experiment 5.3 or ESM RCP8.5 experiment 2006-2100, were forced with projected CO_2 emissions, following only one scenario— RCP8.5 (Moss et al., 2010). We chose the emission-driven runs because the fully coupled ESMs in these runs have interactive carbon cycle component that can simulate climate-carbon cycle feedback mechanisms. Global atmospheric CO_2 concentrations are simulated prognostically, therefore they reflect the total effect of all the physical, chemical, and biological processes on Earth, and their interactions and feedbacks with the climate system. We obtained model output primarily from the Earth System Grid Federation (ESGF), an international network of distributed climate data servers (Williams et al., 2011). For the GFDL model, we directly retrieved the output from GFDL's Data Portal (http://nomads.gfdl.noaa.gov:8080/DataPortal/cmip5.jsp). The main characteristics of the 10 models are listed in Table 1.

2.2 Analysis procedure

We first analyzed the monthly output of prognostic atmospheric CO_2 concentrations to evaluate the change of CO_2 seasonal amplitude (defined as maximum minus minimum of detrended seasonal cycle) from 1961 to 2099. Atmospheric CO_2 was obtained primarily as the area- and pressure-weighted mean of CO_2 across all vertical levels—a better representation of atmospheric carbon content than surface CO_2. The INM-CM4 model does not provide CO_2 concentration, so we converted its total atmospheric mass of CO_2 to mole fraction. We excluded the IPSL model from analyses in Section 3.1 and 3.2 because its CO_2 output is not available. Only CanESM2 provides three different realizations for both historical and future runs, and we simply use its first realization in our comparison. We believe this choice would lead to a more representative result than including all realizations of CanESM2 in multi-model averaging.

To extract the CO_2 seasonal cycle from the monthly records, we applied the curve-fitting procedures using the CCGCRV software developed at the National Oceanic and Atmospheric Administration Climate Monitoring and Diagnostics Laboratory (Thoning et al., 1989; http://www.esrl.noaa.gov/gmd/ccgg/mbl/crvfit/crvfit.html). This algorithm first fits the long-term variations and the seasonal component in the monthly CO_2 record with a combination of a trend function and a series of annual harmonics. Then the residuals are filtered with fast Fourier transform and transformed back to the real domain. Specifically, we followed the default setup of a quadratic polynomial for the trend function, a four-yearly harmonics for the seasonal component, and long/short-term cutoff values of 667 days/80 days for the filtering in our analyses. We examined the phase change of CO_2 detrended seasonal cycle by counting how frequent the maxima and minima occur in different months. We used two definitions of seasonal amplitude in our analyses that yield similar results: one directly comes from the CCGCRV package, and another definition is simply max minus min of detrended seasonal cycle in each year. For each model's monthly global mean CO_2, we first computed the detrended CO_2 seasonal cycle as the annual harmonic part plus the filtered residue using the short-term cutoff value. Then we started to investigate the global carbon budget in each model:

$$\frac{dCO_2}{dt} = FFE - NBP + FOA. \quad (1)$$

The left term is the change of CO_2 concentration (or CO_2 growth rate), which we simply computed as the difference between the current month and previous month's concentration—this leads to a half-month shift earlier than the results indicate. The right side comprises of fossil fuel emission (FFE), net biosphere production (NBP, or net terrestrial-atmosphere carbon exchange, positive if land is a carbon sink) and net ocean-atmosphere flux (FOA, positive if ocean releases carbon). Previous studies have limited the impact of FFE and FOA on trends in CO_2 amplitude to less than a few percent change (Graven et al., 2013). Therefore we focused on examining the seasonal cycle of NBP in this study.

For each model, we checked and ensured that the sum of individual flux terms in equation (1) equals to the CO_2 growth rate. However, further breakdown of NBP may look very different. For example, the GFDL-ESM2m model's NBP has component fluxes including Net Primary

Production (NPP), heterotrophic respiration (R_h), fluxes from land use change (fLuc), fire (fFire), harvest (fHarvest) and grazing (fGrazing). In contrast, NBP approximately equals to NPP minus R_h in CanESM2. To investigate whether the amplitude change is mostly due to enhanced production or respiration, we examined the seasonal cycle of NPP and respiration separately. The INM model does not provide NPP output, so it is excluded in this part of analyses. For respiration, instead of directly adding all flux components such as R_h and fLuc for each model (which would be unnecessary and difficult since not all fluxes are provided), we defined R_h^* (dominated by R_h) such that

$$R_h^* = NPP - NBP. \quad (2)$$

Additionally, we analyzed the spatial patterns of NBP changes between future (2081-2090) and historical (1961-1970) period. We examined the peak seasons of carbon uptake and release by the biosphere, namely May-July and October-December averages, respectively. The difference between the two periods gives us an approximate representation of the spatial patterns of NBP amplitude change. We chose three-month averages for multi-model ensemble, because not all models simulate peak uptake in June and peak release in October. Monthly output of NBP, NPP and R_h^* (derived from NBP and NPP) from all models were first resampled to 2°*2° grids. Then the spatial and zonal means for both May-July and October-December were computed.

3 Results

3.1 Changes of CO_2 and NBP seasonal amplitude

The CMIP5 models project that the increase of CO_2 seasonal amplitude continues in the future. Figure 1a shows detrended and globally averaged monthly column atmospheric CO_2 from 1961 to 2099, averaged over nine models (no IPSL). The models project an increase of CO_2 seasonal amplitude (defined as max minus min in each year) by about 70% over 120 years, from 1.6 ppm during 1961-1970 to 2.7 ppm in 2081-2090. The increase is faster in the future than in the historical period. Another feature is that the trend of minima (−0.63 ppm $Century^{-1}$) has a larger magnitude than the trend of maxima (0.41 ppm $Century^{-1}$), suggesting that enhanced vegetation growth contributes more to the amplitude increase than respiration increase. Gurney and Eckels (2011) found the trend of net flux in dormant season is larger than that of growing season. However, they applied a very different definition for amplitude, considering all months instead of maxima and minima, to analyze the atmospheric CO_2 inversion results from 1980-2008. Specifically, they defined growing season net flux (dormant season net flux) as the total of any month for which the net carbon flux is negative (positive), and amplitude as the difference of the two net fluxes. It is no surprise they reached a conclusion that seems to contradict ours, since growing season is much shorter than dormant season at global scale. Figure 1b and 1c present detrended global mean CO_2 growth rate (1 ppm=2.12 PgC Month^{-1} for unit conversion) and global total −NBP, two quantities showing very similar characteristics as expected. All models simulate an increase in amplitude, although considerable model spread is found (Table 2). In addition, we notice a phase advance of maxima and minima by counting their time of occurrence (data not shown). Excluding models above one standard deviation from the ensemble mean yields similar results.

To illustrate how well the models reproduce the seasonal variations of CO_2, we compared the multi-model ensemble global CO_2 at the lowest model level—not equivalent to the height of surface CO_2 measurement, but relatively close—with ESRL's global mean CO_2 over 1981-2005 (Figure 1d). The surface CO_2 seasonal amplitude increase estimated by the models is lower than that of ESRL's global CO_2 estimate, however the changes of amplitude are similar (Table 3). This surface station-based global CO_2 estimate also indicates that the amplitude increase is dominated by the trend of minima.

We further calculated the change of relative amplitude (relative to 1961-1970) for each model. The amplitude here is computed by the CCGCRV package. As illustrated in Figure 2, all nine models show an increase in the amplitude of both global mean CO_2 and NBP seasonal amplitude. CO_2 seasonal amplitude has increased by 62±19% in 2081-2090, compared to 1961-1970; whereas NBP seasonal amplitude has increased by 68±25% over the same period (see Table 4 for details of individual models). The trend of increase is much higher in the future (CO_2/NBP: 0.70%/0.73% per year during 2006-2099) than in the historical period (0.25% and 0.28% per year during 1961-2005 for CO_2 and NBP), albeit the model spread also becomes larger in the future. When we applied the same procedure to the Northern Hemisphere (25-90°N) mean CO_2 and total NBP for the eight models (excluding INM-CM4 which only has global CO_2 mass), we saw a higher amplitude increase and larger model spread: 81±46% and 77±43% for CO_2 and NBP, respectively.

3.2 Production vs. respiration

Our next question is whether the amplitude change of NBP is largely driven by NPP or respiration. We computed the mean seasonal cycle of detrended CO_2 growth rate, −NBP, −NPP (reverse signs so that negative values always indicate carbon uptake) and R_h* in two periods: 1961-1970 (black) and 2081-2090 (red), for the nine models (for this and following analyses, we excluded INM which does not provide NPP, and included the IPSL model except for CO_2 growth rate). The seasonal cycle of −NBP resembles that of detrended CO_2 growth rate (Figure 3a-d), confirming that the activities of land ecosystem dominate the CO_2 seasonal cycle and its amplitude change in the model simulations. Except for CanESM2 (also noted in Anav et al., 2013), and BNU-ESM (which simulates a second peak carbon uptake around November) to some extent, most models can reproduce the net uptake of carbon during spring and summer (when increasing NPP overcomes respiration) and the net carbon release during fall and winter at global scale: net carbon uptake peaks in June (five models) or July (three models) for the historical period, and exclusively in June for the future period. However, the model spread on amplitude is large: CESM1-BGC and NorESM1-ME, which has the same land model (CLM4) that features an interactive nitrogen cycle, are characterized by a small seasonal amplitude of −NBP — merely 30% of those on the high end of the models (IPSL-CM5A-LR and MPI-ESM-LR). The seasonal amplitude of multi-model ensemble NBP, computed as maximum minus minimum (June-October), has increased from 2.7 PgC Month^{-1} to 4.7 PgC Month^{-1} (Figure 3d). The 2 PgC Month^{-1} amplitude change is the sum of enhanced net carbon uptake in June and higher net release in October, and the uptake increase (1.4 PgC Month^{-1}) is nearly three times as large as the release increase (0.5 PgC Month^{-1}). The biggest increase of carbon uptake mostly takes place during a short period from May to July, while carbon release exhibits a longer period of smoothed change from August to January.

We then investigate the June and October changes of −NPP and R_h^*, respectively. By definition, their sum should equal to the amplitude change of −NBP. NPP has increased in all months (Figure 3e, f), with much larger changes during the Northern Hemisphere growing season. The amplitude of multi-model ensemble NPP has increased from 4.8 PgC Month^{-1} to 7.1 PgC Month^{-1}, and an increase from 2.7 to 4.3 PgC Month^{-1} is found for R_h^*. In June, NPP increase (4.5 PgC Month^{-1}) is larger than that of R_h* (3.1 PgC Month^{-1}), resulting in enhanced net uptake. In October, NPP increase (1.9 PgC Month^{-1}) is smaller than that of R_h*

(2.4 PgC $Month^{-1}$), leading to enhanced net release. These results are consistent with trends of maxima and minima in Figure 1.The models also indicate a shift in peak NPP from July to June, consistent with the shift of CO_2 minima.

3.3 Spatial and latitudinal contributions

To further investigate the regional contribution to NBP change, we plotted the 10-model mean −NBP changes (Figure 4) over peak Northern Hemisphere growing season (May-July, panel a) and dormant season (October-December, panel b). Because the models disagree on the time of maximum and minimum NBP (Figure 3), our choice of doing seasonal averages would be more representative of the models than averaging over one month. Only CanESM2, which has serious problems reproducing NBP seasonal cycle (also noted in Anav et al., 2013), have a peak uptake outside May-July for the historical period. Net carbon release of most models plateaued from late fall to early spring, and October-December mean is a reasonable representation of the dormant season. Note that the difference between the two seasonal averages is smaller than the peak-to-trough amplitude, but for our purpose of examining relative spatial contribution, this difference can be neglected. We saw stronger net carbon uptake in May-July almost everywhere north of 45°N, and also over the Tibetan Plateau and some places near equator. Net carbon uptake weakens over Western United States and Central America, South and Southeast Asia and Central South America. The change of net carbon release in October-December generally shows an opposite spatial pattern, but the relative magnitude of change north of 45°N is much smaller.

In addition, we calculated the zonal averages of the changes (panel c) in May-July (black line) and October-December (red line). The green shaded areas contribute positively to the amplitude increase, whereas the yellow shades contribute negatively. The area-weighted totals of the three-month averaged zonal mean curves correspond to the future (red) minus historical (black) three-month averages of global total −NBP (Figure 3d), for May-July and October-December, respectively. These two curves do not account for phase difference; instead, they approximate latitudinal contribution to the amplitude change of global total −NBP. It is apparent that the seasonal amplitude increase of NBP is dominated by regions north of 45°N with a weak contribution from the Southern Hemisphere tropics (25°S-0°). The Northern subtropical region and Southern Hemisphere (10-30°N, 55-35°S) partly offset the amplitude increase. It is also clear that the amplitude increase is dominated by changes in peak growing season (larger green shade left of the zero line), consistent with our findings in the previous section.

Analogous to the cold-warm seasonality in the temperate/boreal region, the tropics has distinctive dry and wet seasons, and recently Wang et al. (2014) suggested the tropical ecosystem is becoming more sensitive to climate change. In our analyses on the multi-model ensemble patterns, the tropical region exhibits a small negative contribution to the seasonal amplitude increase of global total −NBP. This does not mean the net carbon flux in the tropics, which has a different seasonal cycle phase, would experience an amplitude decrease in the future. To illustrate the seasonal amplitude change at different latitudes, we show the zonal amplitude of NBP in the historical (black) and future (red) periods for all models (Figure 5). At every 2-degree band, we first calculated a ten-year mean seasonal cycle, then compute its amplitude (maximum minus minimum). Most models predict an increase in NBP seasonal amplitude at almost every latitude under the RCP85 emission scenario. Two of the models, CanESM2 and MIROC-ESM, predict decreased seasonality for parts of the tropics and subtropics. Unlike in Figure 4c, an area-weighted integral cannot be performed due to different phases zonally. The Southern Hemisphere has an opposite phase from its Northern counterpart, but its magnitude is small due to its small land area. The two subtropical maxima around 10°N and 10-15°S reflect the wet-dry seasonal shift in the Inter-Tropical Convergence Zone (ITCZ) and monsoon movement. They are comparable to the Northern Hemisphere maxima in terms of both amplitude and amplitude increase for about a third of the models, however they are out of phase and largely cancel each other out.

To further illustrate this cancelation effect, we aggregated monthly −NBP over six large regions: the globe (90°S-90°N), Northern boreal (50-90°N), Northern temperate (25-50°N), Northern tropics (0-25°N), Southern tropics (25°S-0°) and Southern Hemisphere (90-25°S) (Figure S1). It is clear that the changes of global –NBP seasonal cycle mostly come from changes in the Northern boreal region; changes in the Northern temperature regions are also important in a few models. The seasonal cycle of the Northern tropics is characterized by spring maxima and fall minima, and prominent increases of its seasonal amplitude are found for BNU-ESM, GFDL-ESM2M and IPSL-CM5A-LR. However, these changes are largely counterbalanced by changes in the Southern tropics. For GFDL-ESM2M, changes in the Southern tropics are larger than its Northern counterpart, but even so, the net contribution of tropical regions to its global −NBP seasonal amplitude (September maxima minus June minima) change is limited to about 25%, the largest of all models.

3.4 Mechanisms for amplitude increase

As discussed in Section 1, two major mechanisms for amplitude increase identified in previous literature are CO_2 fertilization effect and high latitudes "greening" in a warmer climate. Both mechanisms lead to enhanced ecosystem productivity during peak growing season, and consequently more biomass to decompose in dormant season, therefore increasing the amplitude of NBP seasonal cycle. Because models have different climate and CO_2 sensitivity (Arora et al., 2013), their relative importance may vary. Sensitivity experiments are usually carried out to investigate the relative contribution of different mechanisms. In the case of CMIP5 ESMs, two additional experiments are recommended: Fixed Feedback 2 (esmFdbk2) and Fixed Climate 2 (esmFixClim2). The former keeps CO_2 concentration fixed but allows physical climate change responding to increasing historical and future (RCP4.5) concentrations; the latter keeps climate fixed under preindustrial CO_2 condition but allows the carbon cycle to respond to historical and future (RCP4.5) CO_2 increase. This setup does not permit quantifying the contribution of CO_2 increase and climate change to NBP amplitude increase: one major difference is the use of RCP4.5 concentrations instead of RCP8.5 emissions. However, we can still make qualitative assessments by examining the spatial patterns. We will focus on the high latitude regions, which contribute most to amplitude increase of global total NBP.

Of the ten models we studied, only CanESM2, GFDL-ESM2M and IPSL-CM5A-LR have submitted NBP output for these two experiments (MIROC submitted output for esmFixClim2 only). Here we first display the spatial patterns of −NBP changes for GFDL-ESM2M (Figure 6) and IPSL-CM5A-LR (Figure 7). CanESM2 results are not shown because it does not correctly reproduce the phase of global total NBP seasonal cycle. The changes of −NBP for both models during peak growing season are clearly dominated by CO_2 fertilization effect (right panels). In contrast, climate change under fixed CO_2 fertilization conditions has mixed effects on high latitude regions. Northern high latitude net carbon release in October-December is increased both under climate change (Figure 6c) and elevated CO_2 conditions

(Figure 6d) for GFDL-ESM2M, but over different regions. For IPSL-CM5A-LR however, net carbon release increase in regions north of 45°N is only obvious under elevated CO_2 condition.

Our results only indicate CO_2 fertilization effect is the dominant factor for NBP seasonal amplitude increase in some models. For models with strong carbon-climate feedbacks and weak/moderate water constraints in Northern high latitude regions, climate change may be more important. However, we cannot find a clear example due to data availability. MIROC-ESM is known to have strong carbon-climate feedback (Arora et al., 2013). From its simulation under fixed climate (figure not shown), we found no obvious patterns of widespread net carbon release increase in dormant season, suggesting climate change may play a bigger role for this model. The HadGEM model is another possible candidate; it is also a particularly interesting model to analyze since one of its historical simulations represented the largest change in CO_2 amplitude in Graven et al (2013). Unfortunately, for the ESM simulations, both CO_2 and NBP from HadGEM are not available on the ESGF servers.

3.5 Relationship with mean carbon sink

Our analyses above suggest CO_2 fertilization effect is a major mechanism causing the amplitude increase in some models. If it is important in most models, we expect to see models with a larger change in mean carbon sink simulate a larger change in seasonal amplitude. By plotting the −NBP change against NBP seasonal amplitude change for all 10 models (Figure 8), we found there is indeed a negative cross-model correlation ($R=-0.73$, $p<0.05$), indicating models with a stronger net carbon uptake are likely to simulate a larger increase in NBP seasonal amplitude. Note that this result is based on the 10 models we analyzed; it is subject to large uncertainty and may change substantially with inclusion or exclusion of certain model(s). Again all models show an increase in NBP seasonal amplitude, even though they disagree on the direction of future NBP change. While our study hint at a possible relationship between mean carbon sink and NBP seasonal amplitude, it is beyond our scope to discuss further, or comment on why models show such different mean sink estimate. Interested readers may refer to the insightful discussion on this issue in Friedlingstein et al. (2013).

4 Discussions

We have primarily focused on model ensembles of largely aggregated quantities. It is possible for the ensemble patterns to be dominated by only a few models, particularly since the seasonality varies considerably between the models. However, when we closely examine each individual models, the spatial patterns of −NBP change during peak growing season (May-July) are all dominated by high latitude regions (approximately north of 45°N), although for CESM1-BGC and NorESM1-ME, regions of enhanced net carbon uptake are confined to only about half of the high latitude regions (Figure S2). Models differ on finer details: for example, about half of the models predict an obvious increase of net carbon uptake for the Tibetan Plateau. It is worth mentioning that the esmFixClim2 experiment of MIROC-ESM show little change for this region under fixed climate conditions. High latitude regions also dominate the increase of net carbon release in October-December for most models (Figure S3). One exception is INM-CM4, which displays very small change in the dormant season, and most of its NBP amplitude change comes from enhanced carbon uptake during peak growing season. Note that because BNU-ESM and CanESM2 have some problem reproducing the correct phase of global −NBP seasonal cycle, their panels do not represent their NBP maxima changes. When we exclude these two models, we get very similar spatial and zonal patterns as in Figure 4. Another caveat is we assume 1961-1970 can represent the historical condition, and 2081-2090 can represent the future. This choice is valid if the variables we examined have roughly monotonic trends, and ten years is long enough to smooth out most of the interannual variability. Figure 2 suggests this assumption we used is quite reasonable for model ensembles, and acceptable for individual models.

We presented aggregated quantities due to large model uncertainty in space, and so far, we have largely omitted comparing the models with observations (partly due to limited observation during 1961-1970), which is a major focus in some other studies on CMIP5 (Anav et al., 2013) and some other model intercomparison projects (Peng et al., 2014). Can the models reproduce observed CO_2 seasonal amplitude increase at the two stations with longest observation records—Mauna Loa, Hawaii and Point Barrow, Alaska? If the global increase in CO_2 amplitude is 70% from 1961 to 2090, what does that mean for Mauna Loa and Point Barrow CO_2? To answer these interesting questions, we extracted simulated CO_2 concentration from eight models at their model grid that is closest to Mauna Loa both horizontally and vertically (we performed a similar procedure for Point Barrow CO_2). The results of this comparison at one model grid can reflect multiple sources of model uncertainties, including uncertainties in the atmospheric tracer transport and mixing simulations. GFDL-ESM2M for example, is known to simulate a damped CO_2 gradient (Dunne et al., 2013), and it has long been identified as a deficit in models of the atmospheric CO_2 cycle (Fung et al., 1987). Due to limited observation constraints, such site comparison should be treated with extra caution. Figure 9 (and Figure S4 for more details) present the changes of CO_2 seasonal amplitude from the models and observation at Mauna Loa. Three quarters of the models underestimate the CO_2 seasonal amplitude by a factor of 2. However, the observed amplitude change (0.34±0.07% per year, error range represents one standard error of the least-squared trend calculation) is not far off from the model ensemble (0.36±0.24% per year, error range represents one standard deviation model spread). MPI-ESM-LR can reproduce both the magnitude and change of Mauna Loa CO_2 seasonal amplitude reasonably well. For Point Barrow (Figures 10 and Figure S5), MPI-ESM-LR also simulates an amplitude change similar to observation, but its magnitude is almost twice as large as observed (16.3 ppm). Other models underestimate the amplitude, but for the amplitude change, the model ensemble (0.46±0.21% per year) again is similar to observation (0.43±0.10% per year). MRI-ESM1 is found to reproduce both the magnitude and change of Point Barrow CO_2 seasonal amplitude very well.

It is no surprise that Graven et al. (2013) found the CMIP5 models substantially underestimate the seasonal amplitude of CO_2 north of 45°N at altitude of 3 to 6 km, while we did not find the models underestimate Point Barrow CO_2 seasonal amplitude at surface level. One big difference is the observation data used for comparison. We only compared model simulation with observed CO_2 records at Point Barrow from 1974 to 2005 because continuous in-situ CO_2 measurement at Point Barrow only started after 1974, and historical simulations of CMIP5 ESMs stopped by the end of 2005. During the 1974-2005 period, CO_2 seasonal amplitude increases by 0.43% yr^{-1}, or 21.5% over 50 years at Point Barrow. This is lower than the 0.6% yr^{-1}, or 30% increase derived from measurements of the same station, but from a longer time series with a large gap. Even the 30% increase is much lower than the about 50% amplitude increase computed from the two aircraft campaigns during 1958-1961 and 2009-2011. Could this difference be attributed to some physical mechanisms that affect the vertical profile of CO_2 concentration? It is also not clear to what extent the large interannual variability of CO_2 seasonal amplitude affects the estimation of observed CO_2 amplitude change.

According to the CMIP5 models we analyzed, under the RCP8.5 emission scenario, we would see a 62±19% increase of CO_2 seasonal cycle globally from 1961-1970 to 2081-2090. The increase is larger at Mauna Loa, reaching 85±48% (range indicates one standard deviation model spread), and even larger at Point Barrow, reaching 110±42%. This result should be treated carefully: even though the CMIP5 models are able to reproduce the change of CO_2 seasonal amplitude, some of them rely heavily on the CO_2 fertilization mechanism, which may be too strong compared to observational evidence: previous research suggest it should explain no more than 25% of the observation at a high fertilization effect permitted by lab experiments (Kohlmaier et al., 1989). On the other hand, recent studies have indicated that some important mechanisms, such as changes in ecosystem structure and distribution (Graven et al., 2013) and land use intensification (Zeng et al., 2014), are not represented in the current CMIP5 models. Yet another main source of uncertainty is future CO_2 emission. The RCP8.5 scenario used to drive the ESMs is on the high side of future scenarios. Also, the emission-driven runs simulate higher CO_2 than observed over the historical period, and such biases are likely to increase through time as the atmospheric CO_2 growth rate accelerates (Hoffman et al., 2014).

For the coupled models we studied, even if they have the same strength of carbon-climate feedback, their response to climate change may vary significantly if they simulate very different climate change, adding another layer of complexity. To briefly address this issue, we present soil moisture (Figure S6 and S7) and near-surface temperature (Figure S8 and S9) changes of the three-month means for all models. The models all show temperature increase, but with varying degrees. Models disagree on the spatial pattern of soil moisture change: this difference combined with temperature change and different PFT specifications could generate quite different model behaviors over same regions. Such are important subtleties that highlight the importance of sensitivity experiments and warrants more in-depth future studies.

The combined effect of climate and CO_2 changes not only alters the balance between production and respiration for existing ecosystems, but also lead to changes of ecosystem types. Figure 11 shows tree fraction has increased over wide areas of the Northern high latitude regions for MPI-ESM-LR and INM-CM4, and figure 12 reveals notable increase over the Northern high latitude regions for BNU-ESM. Such widespread vegetation change has not been observed during the satellite era, and it is possibly yet another highly uncertain mechanism contributing to amplitude change in some CMIP5 models.

Finally, we will wrap up our discussion with the impact of land use/land cover change on CO_2 NBP seasonal amplitude. The major crops are characterized by high productivity in a short growing season, and they tend to have a larger NBP seasonal amplitude compared to the natural vegetation they replace, usually natural grass. An increase in cropland fraction over high latitude regions could contribute to the seasonal ampltiude increase of NBP. As far as we know, no CMIP5 model has accounted for agricultural intensification, and only some models have implemented a conversion matrix (Brovkin et al., 2013). Therefore, the most important change implemented in the CMIP5 models is fractional land cover change based on Hurtt et al. (2011). In Figure S10 we present the change of crop fraction, available from five models. It is apparent that crop area has increased mostly in the Tropics, while regions north of 30N has actually seen a decrease (due to a variety of factors: cropland abandonment, reforestation, urbanization, etc.). Therefore, crop fractional cover change alone may decrease the NBP seasonal amplitude in CMIP5 simulations. A better representation of land use change, especially the agricultural intensification, is needed in CMIP5 models to represent the CO_2 and NBP seasonal cycle better. On a side note, the other major part of land cover change—pasture (often treated as natural grass in ESMs, Brovkin et al., 2013) fraction change is unlikely to have a significant effect on NBP seasonal amplitude in the CMIP5 simulations.

5 Conclusions

Under the RCP8.5 emission scenario, all models we examined project an increase in seasonal amplitude of both CO_2 and NBP. In addition, the models indicate an earlier onset and peak of Northern Hemisphere biosphere growth and decay under future climate and CO_2 conditions. Our analyses also suggest the amplitude increase is dominated by changes in net primary productivity, and in regions north of 45°N. While we focused on the change of amplitude instead of mean carbon sink (a more frequently discussed topic), our results suggest models simulating a larger mean carbon sink increase are likely to project a larger change in NBP seasonal amplitude. Considerable model spread is found, likely due to different model setup and complexity, different climate conditions simulated by the models, sensitivity to CO_2 and climate and their combined effects, and strength of feedbacks. Our findings indicate factors including enhanced CO_2 fertilization and lengthening of growing season in high-latitude regions outcompetes the loss of biosphere productivity due to possible severe drought and forest degradation in the future, according to the CMIP5 models we studied.

Despite of the model consensus in global CO_2 and NBP seasonal amplitude increase, and a reasonable representation of CO_2 seasonal amplitude change at Mauna Loa and Point Barrow compared to surface in-situ observations, the mechanisms for this amplitude increase are debatable. The existing major mechanism of CO_2 fertilization may be too strong, and factors like ecosystem change and agricultural intensification are under-represented or missing in the CMIP5 ESMs. Future model-intercomparison projects should encourage models to participate in consistent and comprehensive sensitivity experiments. We also need a better understanding of the uncertainties in models, observations, and their comparisons.

Acknowledgements

We acknowledge the World Climate Research Programme's Working Group on Coupled Modelling, which is responsible for CMIP, and we thank the climate modeling groups (listed in Table 1 of this paper) for producing and making available their model output. For CMIP the U.S. Department of Energy's Program for Climate Model Diagnosis and Intercomparison provides coordinating support and led development of software infrastructure in partnership with the Global Organization for Earth System Science Portals. The authors also thank NOAA for providing global mean CO_2 estimates, and Yutong Pan for processing part of CMIP5 model data. We are grateful to the two anonymous reviewers for their helpful comments and suggestions. This research was supported by NOAA (NA10OAR4310248 and NA09NES4400006) and NSF (AGS-1129088).

References

Anav, A., Friedlingstein, P., Kidston, M., Bopp, L., Ciais, P., Cox, P., Jones, C., Jung, M., Myneni, R. and Zhu, Z.: Evaluating the Land and Ocean Components of the Global Carbon Cycle in the CMIP5 Earth System Models, J. Clim., 26(18), 6801–6843, doi:10.1175/JCLI-D-12-00417.1, 2013.

Andres, R. J., Gregg, J. S., Losey, L., Marland, G. and Boden, T. a.: Monthly, global emissions of carbon dioxide from fossil fuel consumption, Tellus B, 63(3), 309–327, doi:10.1111/j.1600-0889.2011.00530.x, 2011.

Arora, V. K., Boer, G. J., Friedlingstein, P., Eby, M., Jones, C. D., Christian, J. R., Bonan, G., Bopp, L., Brovkin, V., Cadule, P., Hajima, T., Ilyina, T., Lindsay, K., Tjiputra, J. F. and Wu, T.: Carbon–Concentration and Carbon–Climate Feedbacks in CMIP5 Earth System Models, J. Clim., 26(15), 5289–5314, doi:10.1175/JCLI-D-12-00494.1, 2013.

Arora, V. K., Scinocca, J. F., Boer, G. J., Christian, J. R., Denman, K. L., Flato, G. M., Kharin, V. V., Lee, W. G. and Merryfield, W. J.: Carbon emission limits required to satisfy future representative concentration pathways of greenhouse gases, Geophys. Res. Lett., 38(5), L05805, doi:10.1029/2010GL046270, 2011.

Bacastow, R. B., Keeling, C. D. and Whorf, T. P.: Seasonal amplitude increase in atmospheric CO2 concetration at Mauna Loa, Hawaii, 1959-1982, J. Geophys. Res., 90(D6), 10529–10540, doi:10.1029/JD090iD06p10529, 1985.

Brovkin, V., Boysen, L., Arora, V. K., Boisier, J. P., Cadule, P., Chini, L., Claussen, M., Friedlingstein, P., Gayler, V., van den Hurk, B. J. J. M., Hurtt, G. C., Jones, C. D., Kato, E., de Noblet-Ducoudré, N., Pacifico, F., Pongratz, J. and Weiss, M.: Effect of Anthropogenic Land-Use and Land-Cover Changes on Climate and Land Carbon Storage in CMIP5 Projections for the Twenty-First Century, J. Clim., 26(18), 6859–6881, doi:10.1175/JCLI-D-12-00623.1, 2013.

Buermann, W., Lintner, B. R., Koven, C. D., Angert, A., Pinzon, J. E., Tucker, C. J. and Fung, I. Y.: The changing carbon cycle at Mauna Loa Observatory, Proc. Natl. Acad. Sci. U. S. A., 104(11), 4249–4254, 2007.

Cleveland, W., Freeny, A. E. and Graedel, T. E.: The Seasonal Component of Atmospheric CO2: Information From New Approaches to the Decomposition of Seasonal Time Series, J. Geophys. Res., 88(C15), 10934–10946, 1983.

Conway, T. J., Tans, P. P., Waterman, L. S., Thoning, K. W., Kitzis, D. R., Masarie, K. A. and Zhang, N.: Evidence for interannual variability of the carbon cycle from the National Oceanic and Atmospheric Administration / Climate Monitoring and Diagnostics Laboratory Global Air Sampling Network, J. Geophys. Res., 99(D11), 22831–22855, 1994.

Dufresne, J.-L., Foujols, M. -a., Denvil, S., Caubel, A., Marti, O., Aumont, O., Balkanski, Y., Bekki, S., Bellenger, H., Benshila, R., Bony, S., Bopp, L., Braconnot, P., Brockmann, P., Cadule, P., Cheruy, F., Codron, F., Cozic, A., Cugnet, D., Noblet, N., Duvel, J.-P., Ethé, C., Fairhead, L., Fichefet, T., Flavoni, S., Friedlingstein, P., Grandpeix, J.-Y., Guez, L., Guilyardi, E., Hauglustaine, D., Hourdin, F., Idelkadi, A., Ghattas, J., Joussaume, S., Kageyama, M., Krinner, G., Labetoulle, S., Lahellec, A., Lefebvre, M.-P., Lefevre, F., Levy, C., Li, Z. X., Lloyd, J., Lott, F., Madec, G., Mancip, M., Marchand, M., Masson, S., Meurdesoif, Y., Mignot, J., Musat, I., Parouty, S., Polcher, J., Rio, C., Schulz, M., Swingedouw, D., Szopa, S., Talandier, C., Terray, P. and Viovy, N.: Climate change projections using the IPSL-CM5 Earth System Model: from CMIP3 to CMIP5, Clim. Dyn., 40(9-10), 2123–2165, doi:10.1007/s00382-012-1636-1, 2013.

Dunne, J. P., John, J. G., Shevliakova, E., Stouffer, R. J., Krasting, J. P., Malyshev, S. L., Milly, P. C. D., Sentman, L. T., Adcroft, A. J., Cooke, W., Dunne, K. A., Griffies, S. M., Hallberg, R. W., Harrison, M. J., Levy, H., Wittenberg, A. T., Phillips, P. J. and Zadeh, N.: GFDL's ESM2 Global Coupled Climate–Carbon Earth System Models. Part II: Carbon System Formulation and Baseline Simulation Characteristics*, J. Clim., 26(7), 2247–2267, doi:10.1175/JCLI-D-12-00150.1, 2013.

Friedlingstein, P., Meinshausen, M., Arora, V. K., Jones, C. D., Anav, A., Liddicoat, S. K. and Knutti, R.: Uncertainties in CMIP5 climate projections due to carbon cycle feedbacks, J. Clim., 27, 511–526, doi:10.1175/JCLI-D-12-00579.1, 2013.

Fung, I. Y., Tucker, C. J. and Prentice, K. C.: Application of Advanced Very High Resolution Radiometer vegetation index to study atmosphere-biosphere exchange of CO2, J. Geophys. Res., 92(D3), 2999–3015, doi:10.1029/JD092iD03p02999, 1987.

Graven, H. D., Keeling, R. F., Piper, S. C., Patra, P. K., Stephens, B. B., Wofsy, S. C., Welp, L. R., Sweeney, C., Tans, P. P., Kelley, J. J., Daube, B. C., Kort, E. a, Santoni, G. W. and Bent, J. D.: Enhanced Seasonal Exchange of CO2 by Northern Ecosystems Since 1960., Science, 341, 1085–1089, doi:10.1126/science.1239207, 2013.

Gurney, K. R. and Eckels, W. J.: Regional trends in terrestrial carbon exchange and their seasonal signatures, Tellus B, 63(3), 328–339, doi:10.1111/j.1600-0889.2011.00534.x, 2011.

Hoffman, F. M., Randerson, J. T., Arora, V. K., Bao, Q., Cadule, P., Ji, D., Jones, C. D., Kawamiya, M., Khatiwala, S., Lindsay, K., Obata, A., Shevliakova, E., Six, K. D., Tjiputra, J. F., Volodin, E. M. and Wu, T.: Causes and implications of persistent atmospheric carbon dioxide biases in Earth System Models, J. Geophys. Res. Biogeosciences, 119(2), 141–162, doi:10.1002/2013JG002381, 2014.

Hurtt, G. C., Chini, L. P., Frolking, S., Betts, R. a, Feddema, J., Fischer, G., Fisk, J. P., Hibbard, K., Houghton, R. a, Janetos, a, Jones, C. D., Kindermann, G., Kinoshita, T., Klein Goldewijk, K., Riahi, K., Shevliakova, E., Smith, S., Stehfest, E., Thomson, a, Thornton, P., Van Vuuren, D. P. and Wang, Y. P.: Harmonization of land-use scenarios for the period 1500-2100: 600 years of global gridded annual land-use transitions, wood harvest, and resulting secondary lands, Clim. Change, 109(1), 117–161, doi:10.1007/s10584-011-0153-2, 2011.

Ilyina, T., Six, K. D., Segschneider, J., Maier-reimer, E., Li, H. and Núñez-Riboni, I.: Global ocean biogeochemistry model HAMOCC : Model architecture and performance as component of the MPI-Earth system model in different CMIP5 experimental realizations, J. Adv. Model. Earth Syst., 5, 287–315, doi:10.1029/2012MS000178, 2013.

International Panel on Climate Change: Climate Change 2013: the Physical Science Basis. Working Group 1 Contribution to the Fifth Assessment Report of the International Panel on Climate Change International Panel on Climate Change, Cambridge University Press, Cambridge, New York., 2013.

Ji, D., Wang, L., Feng, J., Wu, Q., Cheng, H., Zhang, Q., Yang, J., Dong, W., Dai, Y., Gong, D., Zhang, R.-H., Wang, X., Liu, J., Moore, J. C., Chen, D. and Zhou, M.: Description and basic evaluation of BNU-ESM version 1, Geosci. Model Dev. Discuss., 7(2), 1601–1647, doi:10.5194/gmdd-7-1601-2014, 2014.

Keeling, C. D., Chin, J. F. S. and Whorf, T. P.: Increased activity of northern vegetation inferred from atmospheric CO2 measurements, Nature, 382, 146–149, doi:10.1038/382146a0, 1996.

Keeling, C. D., Whorf, T. P., Wahlen, M. and van der Plichtt, J.: Interannual extremes in the rate of rise of atmospheric carbon dioxide since 1980, Nature, 375, 666–670, doi:10.1038/375666a0, 1995.

Kohlmaier, G. H., Siré, E. O., Janecek, A., Keeling, C. D., Piper, S. C. and Revelle, R.: Modelling the seasonal contribution of a CO2 fertilization effect of the terrestrial vegetation to the amplitude increase in atmospheric CO2 at Mauna Loa Observatory, Tellus Ser. B-Chemical Phys. Meteorol., 41, 487–510, doi:10.1111/j.1600-0889.1989.tb00137.x, 1989.

Long, M. C., Lindsay, K., Peacock, S., Moore, J. K. and Doney, S. C.: Twentieth-Century Oceanic Carbon Uptake and Storage in CESM1(BGC)*, J. Clim., 26(18), 6775–6800, doi:10.1175/JCLI-D-12-00184.1, 2013.

McGuire, A. D., Sitch, S., Clein, J. S., Dargaville, R., Esser, G., Foley, J., Heimann, M., Joos, F., Kaplan, J., Kicklighter, D. W., Meier, R. a, Melillo, J. M., Moore III, B., Prentice, I. C., Ramankutty, N., Reichenau, T., Schloss, A., Tian, H., Williams, L. J. and Wittenberg, U.: Carbon balance of the terrestrial biosphere in the twentieth century: Analyses of CO2, climate and land use effects with four process-based ecosystem models, Global Biogeochem. Cycles, 15(1), 183–206, 2001.

Moss, R. H., Edmonds, J. a, Hibbard, K. a, Manning, M. R., Rose, S. K., van Vuuren, D. P., Carter, T. R., Emori, S., Kainuma, M., Kram, T., Meehl, G. a, Mitchell, J. F. B., Nakicenovic, N., Riahi, K., Smith, S. J., Stouffer, R. J., Thomson, A. M., Weyant, J. P. and Wilbanks, T. J.: The next generation of scenarios for climate change research and assessment., Nature, 463, 747–756, doi:10.1038/nature08823, 2010.

Pearman, G. I. and Hyson, P.: The annual variation of atmospheric CO2 concentration Observed in the Northern Hemisphere, J. Geophys. Res., 86, 9839–9843, 1981.

Peng, S., Ciais, P., Piao, S., Zeng, N. and Zhao, F.: Benchmarking the seasonal cycle of CO2 fluxes simulated by terrestrial ecosystem models, Global Biogeochem. Cycles, under review, 2014.

Peylin, P., Law, R. M., Gurney, K. R., Chevallier, F., Jacobson, a. R., Maki, T., Niwa, Y., Patra, P. K., Peters, W., Rayner, P. J., Rödenbeck, C., van der Laan-Luijkx, I. T. and Zhang, X.: Global atmospheric carbon budget: results from an ensemble of atmospheric CO_2 inversions, Biogeosciences, 10(10), 6699–6720, doi:10.5194/bg-10-6699-2013, 2013.

Piao, S., Sitch, S., Ciais, P., Friedlingstein, P., Peylin, P., Wang, X., Ahlström, A., Anav, A., Canadell, J. G., Cong, N., Huntingford, C., Jung, M., Levis, S., Levy, P. E., Li, J., Lin, X., Lomas, M. R., Lu, M., Luo, Y., Ma, Y., Myneni, R. B., Poulter, B., Sun, Z., Wang, T., Viovy, N., Zaehle, S. and Zeng, N.: Evaluation of terrestrial carbon cycle models for their response to climate variability and to CO2 trends, Glob. Chang. Biol., 19(7), 2117–2132, doi:10.1111/gcb.12187, 2013.

Randerson, J. T., Field, C. B., Fung, I. Y. and Tans, P. P.: Increases in early season ecosystem uptake explain recent changes in the seasonal cycle of atmospheric CO 2 at high northern latitudes, Geophys. Res. Lett., 26(17), 2765–2768, doi:10.1029/1999GL900500, 1999.

Randerson, J. T., Thompson, M. V, Conway, T. J., Fung, I. Y., Field, C. B., Randerson, T., Thompson, V., Conway, J. and Field, B.: The contribution of terrestrial sources and sinks to trends in the seasonal cycle of atmospheric carbon dioxide, Global Biogeochem. Cycles, 11(4), 535–560, doi:10.1029/97gb02268, 1997.

Taylor, K. E., Stouffer, R. J. and Meehl, G. a.: An Overview of CMIP5 and the Experiment Design, Bull. Am. Meteorol. Soc., 93(4), 485–498, doi:10.1175/BAMS-D-11-00094.1, 2012.

Thoning, K. W., Tans, P. P. and Komhyr, W. D.: Atmospheric carbon dioxide at Mauna Loa Observatory: 2. Analysis of the NOAA GMCC data, 1974–1985, J. Geophys. Res., 94(D6), 8549, doi:10.1029/JD094iD06p08549, 1989.

Tjiputra, J. F., Roelandt, C., Bentsen, M., Lawrence, D. M., Lorentzen, T., Schwinger, J., Seland, Ø. and Heinze, C.: Evaluation of the carbon cycle components in the Norwegian Earth System Model (NorESM), Geosci. Model Dev., 6, 301–325, doi:10.5194/gmd-6-301-2013, 2013.

Volodin, E. M., Dianskii, N. a. and Gusev, A. V.: Simulating present-day climate with the INMCM4.0 coupled model of the atmospheric and oceanic general circulations, Izv. Atmos. Ocean. Phys., 46, 414–431, doi:10.1134/S000143381004002X, 2010.

Wang, X., Piao, S., Ciais, P., Friedlingstein, P., Myneni, R. B., Cox, P., Heimann, M., Miller, J., Peng, S., Wang, T., Yang, H. and Chen, A.: A two-fold increase of carbon cycle sensitivity to tropical temperature variations, Nature, 506, 212–215, doi:10.1038/nature12915, 2014.

Watanabe, S., Hajima, T., Sudo, K., Nagashima, T., Takemura, T., Okajima, H., Nozawa, T., Kawase, H., Abe, M., Yokohata, T., Ise, T., Sato, H., Kato, E., Takata, K., Emori, S. and Kawamiya, M.: MIROC-ESM 2010: model description and basic results of CMIP5-20c3m experiments, Geosci. Model Dev., 4, 845–872, doi:10.5194/gmd-4-845-2011, 2011.

Williams, D. N., Taylor, K. E., Cinquini, L., Evans, B., Kawamiya, M., Lawrence, B. N. and Middleton, D. E.: The Earth System Grid Federation : Software Framework Supporting CMIP5 Data Analysis and Dissemination, CLIVAR Exchanges, 16, 40–42, 2011.

Yukimoto, S., Yoshimura, H., Hosaka, M., Sakami, T., Tsujino, H., Hirabara, M., Tanaka, T. Y., Deushi, M., Obata, A., Nakano, H., Adachi, Y., Shindo, E., Yabu, S., Ose, T. and Kitoh, A.: Meteorological Research Institute-Earth System Model Version 1 (MRI-ESM1), Tech. Reports, 64, Meteorological Research Institute, 2011.

Zeng, N., Zhao, F., Collatz, G. J., Kalnay, E., Salawitch, R. J., West, T. O. and Guanter, L.: Agricultural Green Revolution as a driver of increasing atmospheric CO2 seasonal amplitude, Nature, accepted, 2014.

Zimov, S. A., Davidov, S. P., Zimova, G. M., Davidova, A. I., Chapin, F. S., Chapin, M. C. and Reynolds, J. F.: Contribution of Disturbance to Increasing Seasonal Amplitude of Atmospheric CO2, Science, 284, 1973–1976, doi:10.1126/science.284.5422.1973, 1999.

Table 1. List of Models used and their characteristics

Models	Modeling Center	Land Component	Resolution (Lon x Lat)	Reference
BNU-ESM	Beijing Normal University, China	CoLM3	2.8125° × 2.8125°	(Ji et al., 2014)
CanESM2	Canadian Centre for Climate Modeling and Analysis, Canada	CTEM	2.8125° × 2.8125°	(Arora et al., 2011)
CESM1-BGC	Community Earth System Model Contributors, NSF-DOE-NCAR, USA	CLM4	1.25° × 0.9°	(Long et al., 2013)
GFDL-ESM2m	NOAA Geophysical Fluid Dynamics Laboratory, USA	LM3	2.5° × 2°	(Dunne et al., 2013)
INM-CM4	Institute for Numerical Mathematics, Russia		2° × 1.5°	(Volodin et al., 2010)
IPSL-CM5A-LR	Institut Pierre-Simon Laplace, France	ORCHIDEE	3.75° × 1.875°	(Dufresne et al., 2013)
MIROC-ESM	Japan Agency for Marine-Earth Science and Technology, Atmosphere and Ocean Research Institute (University of Tokyo), and National Institute for Environmental Studies, Japan	MATSIRO + SEIB-DGVM	2.8125° × 2.8125°	(Watanabe et al., 2011)
MPI-ESM-LR	Max Planck Institute for Meteorology, Germany	JSBACH	2.8125° × 2.8125°	(Ilyina et al., 2013)
MRI-ESM1	Meteorological Research Institute, Japan	HAL	1.125° × 1.125°	(Yukimoto et al., 2011)
NorESM1-ME	Norwegian Climate Centre, Norway	CLM4	2.5° × 1.875°	(Tjiputra et al., 2013)

Table 2. Amplitude (max minus min) of global mean column atmospheric CO_2, CO_2 growth rate (CO_2g) and global total NBP, averaged over 1961-1970 and 2081-2090 for the nine models, and their multi-model ensemble (MME) and standard deviation (SD).

Models	CO_2 (ppm)		CO_2g (PgC Month^{-1})		−NBP (PgC Month^{-1})	
	1961-1970	2081-2090	1961-1970	2081-2090	1961-1970	2081-2090
BNU-ESM	1.54	2.96	2.2	4.91	1.88	4.42
CanESM2	0.9	1.53	1.12	2.05	1.2	1.83
CESM1-BGC	1.2	1.76	1.51	2.59	1.6	2.38
GFDL-ESM2m	2.37	3.81	3.42	5.93	3.52	6.24
INM-CM4	0.27	0.41	0.38	0.57	0.3	0.49
MIROC-ESM	2.55	3.92	3.93	5.98	3.77	5.37
MPI-ESM-LR	3.45	5.47	4.35	6.37	4.61	7.51
MRI-ESM1	1.97	4.04	2.37	5.21	2.63	5.7
NorESM1-ME	1.23	1.8	1.6	2.63	1.74	2.73
MME[*]	1.72	2.86	2.32	4.03	2.36	4.07
SD	0.97	1.59	1.34	2.09	1.38	2.33

[*]The multi-model ensemble (MME) here is a simple average over the nine models in the table. The values are slightly larger than given in text because of averaging method (in the main text, multi-model averaging of detrended variables are done first, then their amplitude are computed and mean amplitude changes are derived).

Table 3. Amplitude change (ppm) and trends of maxima/minima of surface CO_2 from eight models, their multi-model ensemble (MME), and ESRL's Global mean CO_2 (CO_2GL).

Models	1981-1985 (ppm)	2001-2005 (ppm)	Percent Change	Trend of Minima (ppm $10yr^{-1}$)	Trend of Maxima (ppm $10yr^{-1}$)
BNU-ESM	2.71	3.1	14.39%	−0.099	0.096
CanESM2	3.04	3.24	6.58%	−0.064	0.02
CESM1-BGC	2.05	2.18	6.34%	−0.032	0.044
GFDL-ESM2m	3.71	3.76	1.35%	−0.033	0.095
MIROC-ESM	3.39	3.61	6.49%	−0.078	0.045
MPI-ESM-LR	6.19	7.02	13.41%	−0.25	0.171
MRI-ESM1	3.69	3.85	4.34%	−0.095	0.031
NorESM1-ME	2.37	2.47	4.22%	−0.024	0.016
MME	3.1	3.37	8.71%	−0.084	0.065
CO_2GL	4.11	4.4	7.06%	−0.102	0.024

Table 4. Column atmospheric CO_2 and NBP amplitude (computed by CCGCRV, slightly different from max minus min) Increases of nine models by 2081-90 relative to their 1961-1970 values and their multi-model ensemble (MME).

Models	CO_2	NBP
BNU-ESM	93%	113%
CanESM2	65%	47%
CESM1-BGC	46%	47%
GFDL-ESM2m	57%	79%
INM-CM4	51%	67%
MIROC-ESM	52%	39%
MPI-ESM-LR	54%	58%
MRI-ESM1	99%	106%
NorESM1-ME	45%	58%
MME	62%	68%

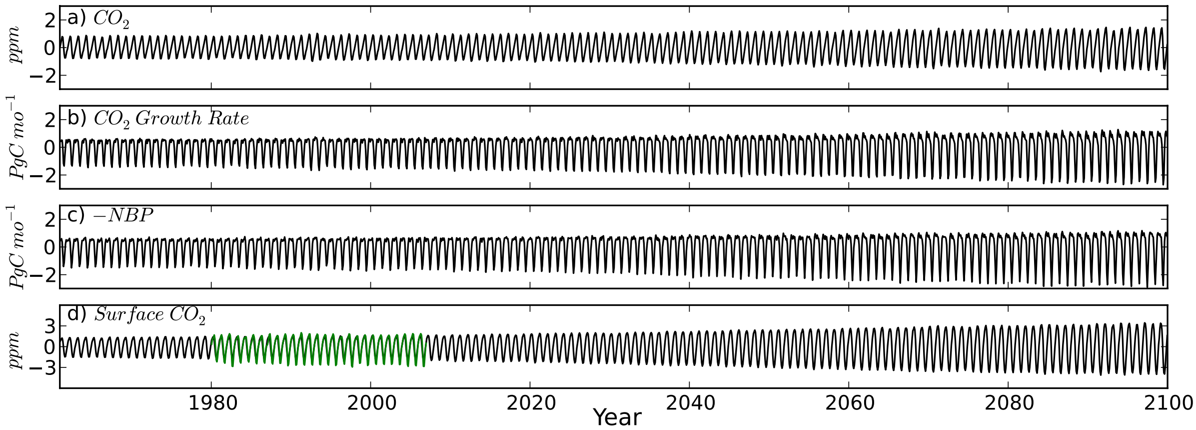

Figure 1. Nine-model (excluding IPSL) averaged monthly detrended a). Global mean CO_2 (ppm, column average); b). Global mean CO_2 growth rate (PgC Month^{-1}, using a conversion factor of 1 ppm = 2.12 PgC Month^{-1}); and c). Global total −NBP (PgC Month^{-1}) from 1961 to 2099. Panel d) presents eight-model (excluding IPSL and INM) averaged monthly detrended global mean CO_2 (ppm) at lowest model level and ESRL's global mean detrended surface CO_2 observation (shown in green).

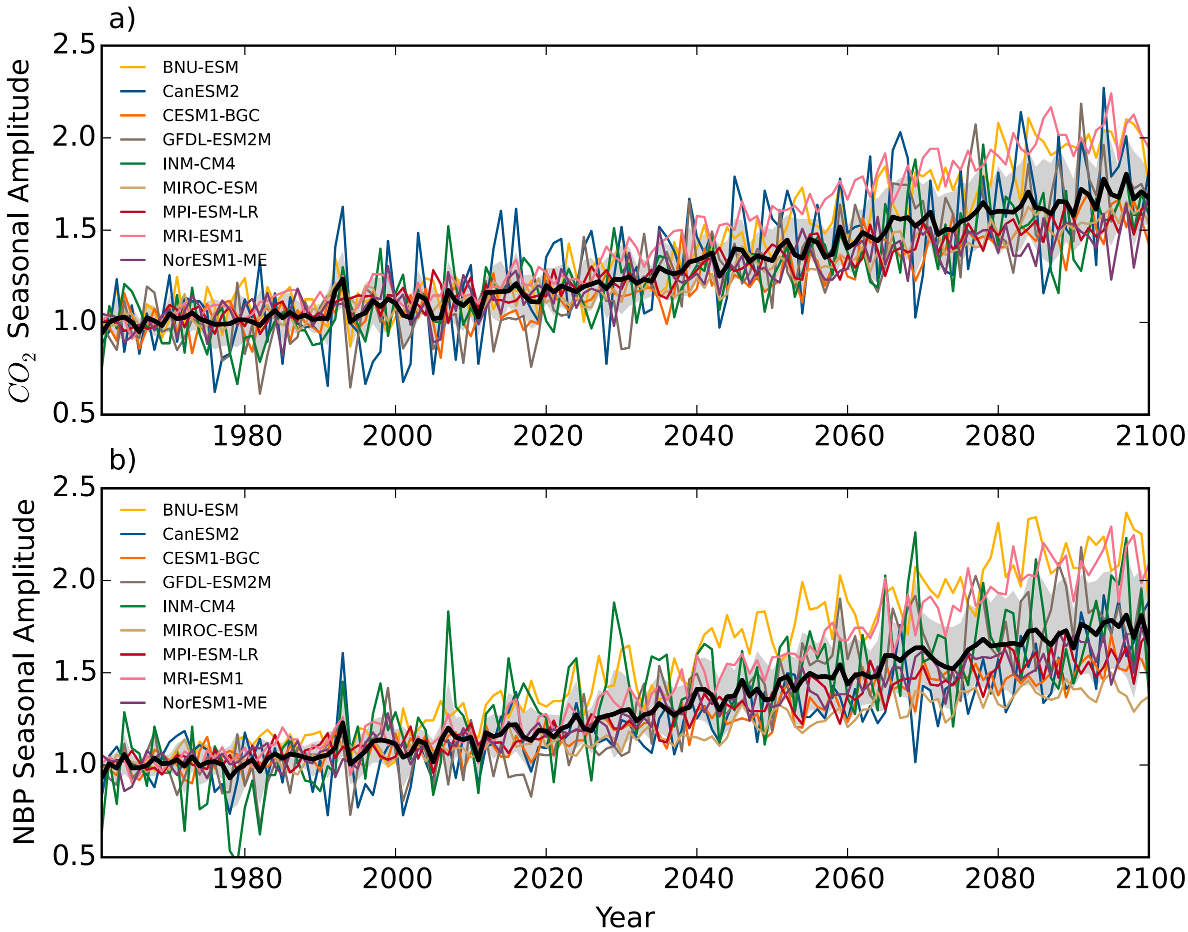

Figure 2. Time series of the relative seasonal amplitude (relative to 1961-1970 mean) of a). Global mean atmospheric CO_2; and b). Global total NBP from 1961 to 2099. Thick black line represents multi-model ensemble, and one standard deviation model spread is indicated by light grey shade.

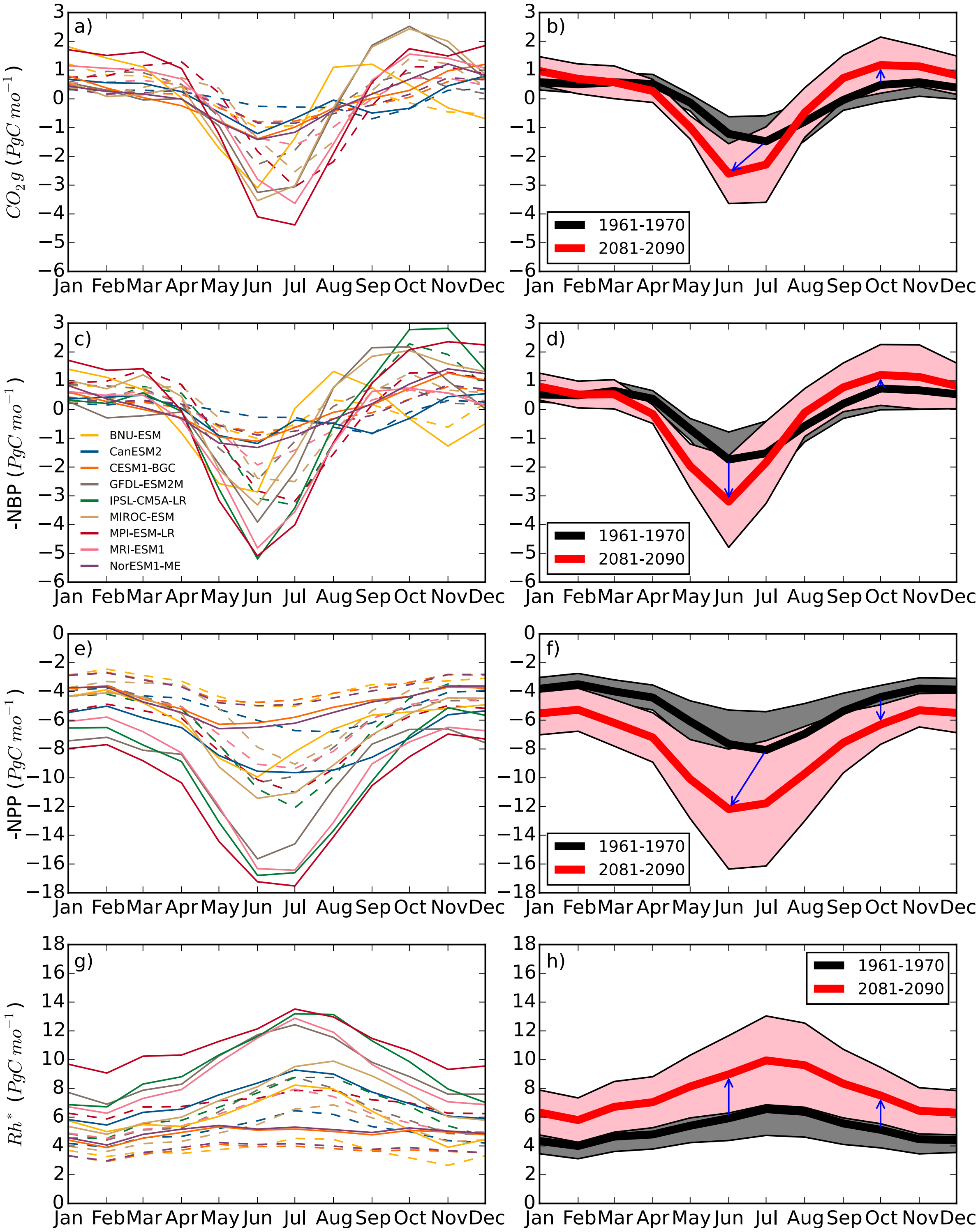

Figure 3. Seasonal cycle of detrended global mean CO_2 growth rate (a, b), global total −NBP (c, d), global total −NPP (e, f), and global total R_h^* (g, h, computed as NPP minus NBP), averaged over 1961-1970 and 2081-2090 for the CMIP5 models (excluding INM, also excluding IPSL for CO_2 growth rate). Seasonal cycle of individual models are presented in the left panel (dashed for 1961-1970, and solid for 2081-2090). Ensemble mean and one

standard deviation model spread (black/grey for 1961-1970, red/pink for 2081-2090) are displayed in the right panels. Blue arrows mark the changes in June and October (NBP maxima and minima), except for CO_2 growth rate and −NPP, where arrows also indicate phase shifts of minima between the two periods. We show −NBP and −NPP so that the negative values represent carbon uptake by the biosphere, and positive values indicate carbon release from the biosphere. Note that −NBP and its two components −NPP and Rh^* are not detrended, so that the sum of panels f and h equals to panel d. Detrended −NBP seasonal cycle (not shown) looks very similar to panel d, as its trend is small compared to the seasonal cycle.

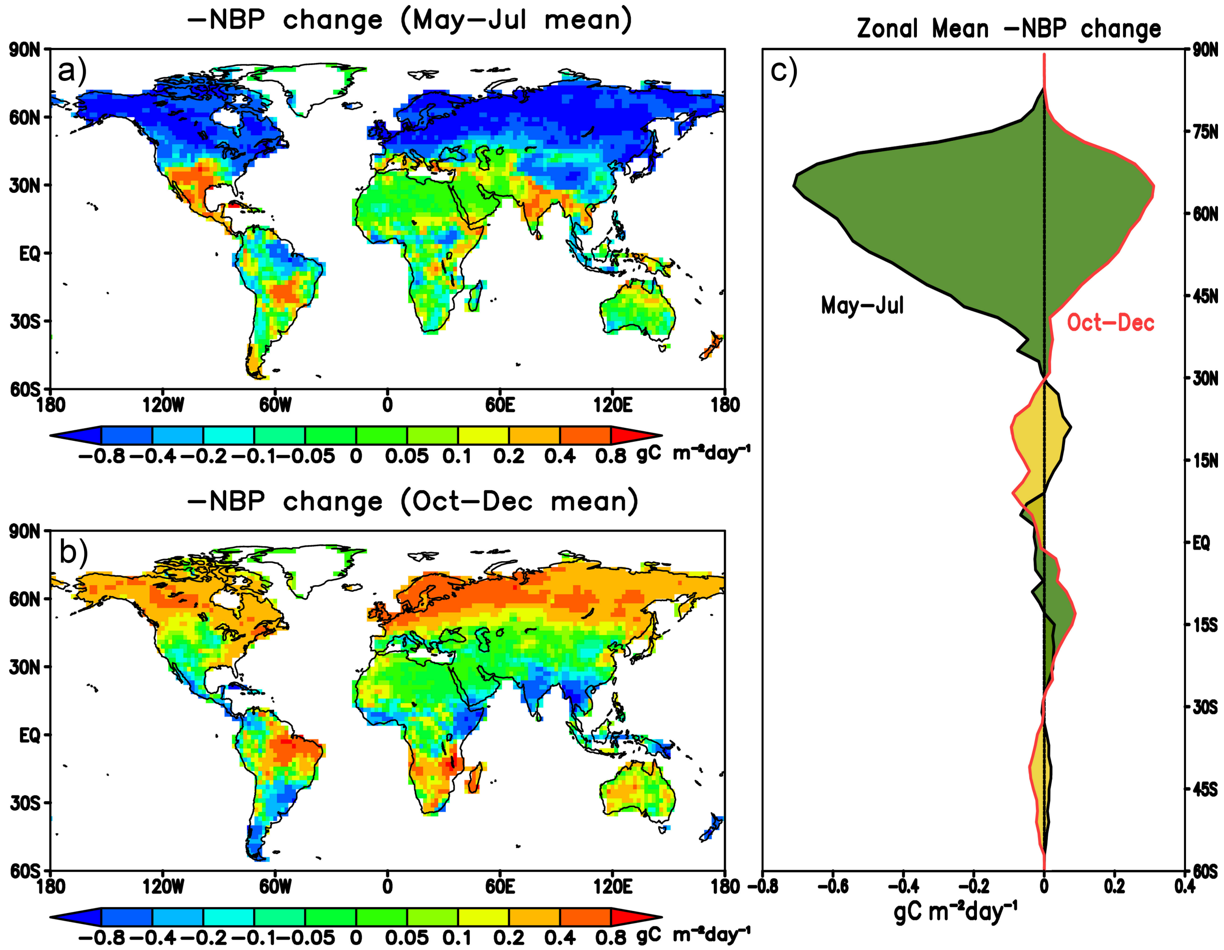

Figure 4. Spatial patterns and Latitudinal distributions of 10-model mean −NBP (gC m^{-2} day^{-1}) changes between 2081-2090 and 1961-1970, during mean a) peak growing season (May-July) and b) dormant season (October-December). Panel c aggregates the spatial patterns in panels a and b zonally, where the black curve corresponds to the −NBP changes in May-July (panel a), and the red curve corresponds to the −NBP changes in October-December (panel b). Further reduction of −NBP in peak growing season—where the black curve falls on the left of the zero line, and increase of −NBP in dormant season—where the red curve is on the right of the zero line, both contribute to amplitude increase. We shade those instances in green, and shade the reversed case (contribute negatively to global total −NBP amplitude increase) in yellow. It is clear that the amplitude increase is dominated by the boreal regions, and by changes in peak growing season.

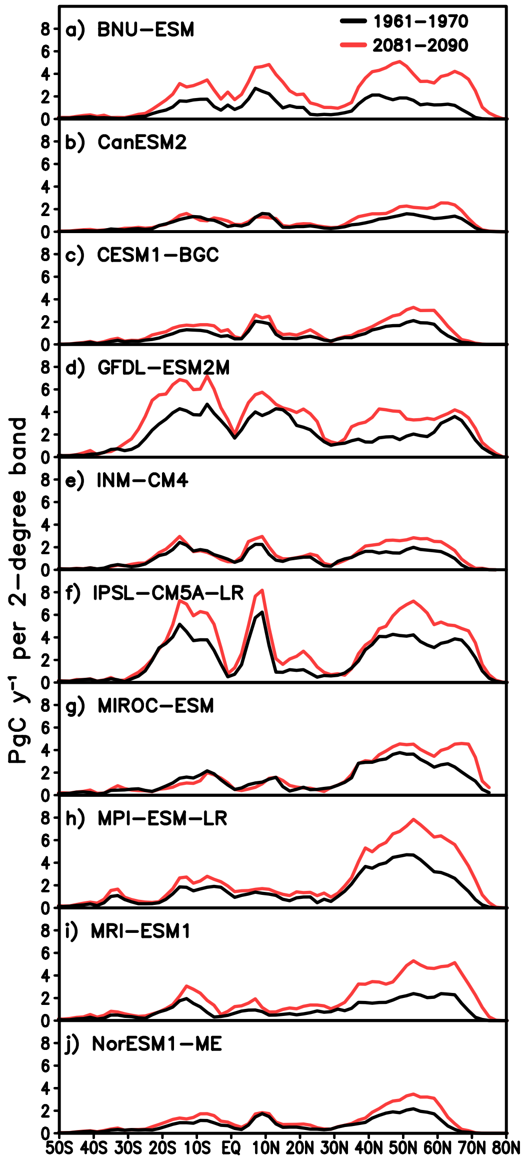

Figure 5. Zonal amplitude of NBP from the 10 CMIP5 models (PgC Month^{-1} per 2-degree band), averaged over 1961-1970 (black) and 2081-2090 (red). For each model, NBP is first regridded to a 2°*2° common grid. Monthly zonal totals are then computed for every 2-degree band, which determine the amplitude (maximum minus minimum) at every band. The Southern Hemisphere has an opposite phase from its northern counterpart, but its magnitude is small due to its small land area. The two subtropical maxima around 10°N and 10-15°S reflect the wet-dry seasonal shift in the Inter-Tropical Convergence Zone (ITCZ) and monsoon movement. They have similar magnitude as the Northern Hemisphere maxima in about a third of the models, however their net contribution to global total NBP seasonal amplitude is small, because they are out of phase and largely cancel each other out.

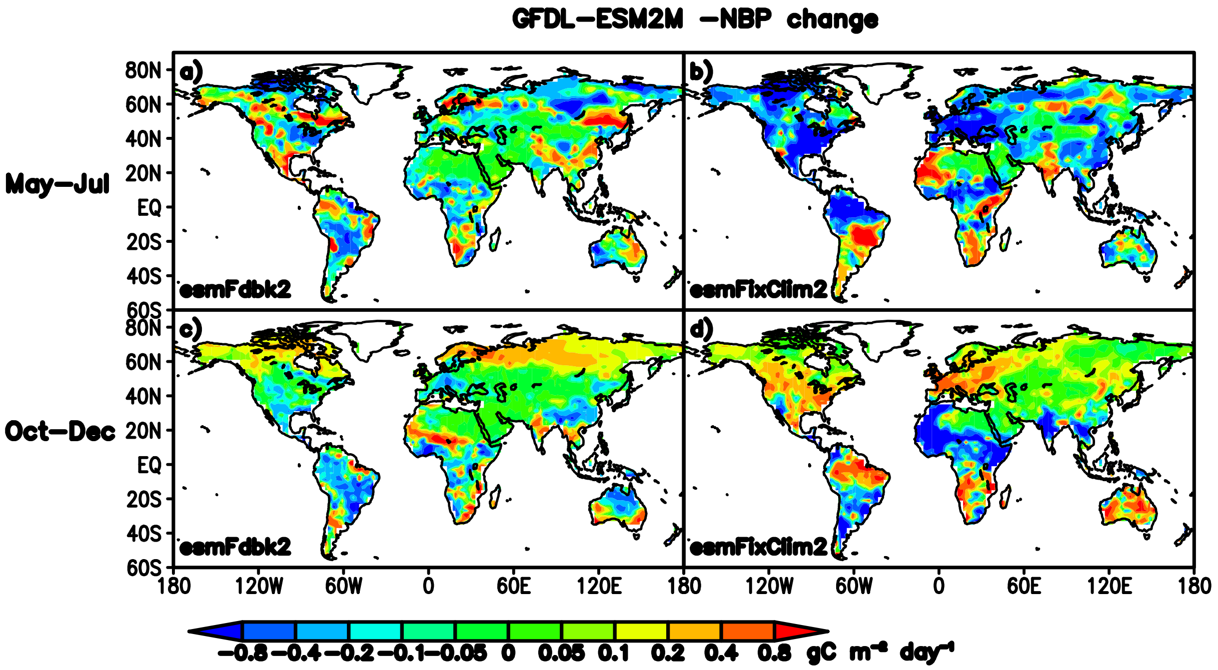

Figure 6. Spatial patterns of GFDL-ESM2M −NBP (gC m^{-2} day^{-1}) changes between 2081-2090 and 1961-1970, during mean peak growing season (May-July, first row) and dormant season (October-December, second row) for the esmFdbk2 (first column, constant CO_2 fertilization and changing climate) and esmFixClim2 (second column, constant climate and rising CO_2) experiments. The Northern high latitude regions show mixed response to climate change during peak growing season (panel a), and most of the Northern temperate and boreal regions see enhanced carbon uptake under elevated CO_2 (panel b). Net carbon release is increased both under climate change (panel c) and elevated CO_2 conditions (panel d), however they have different spatial patterns.

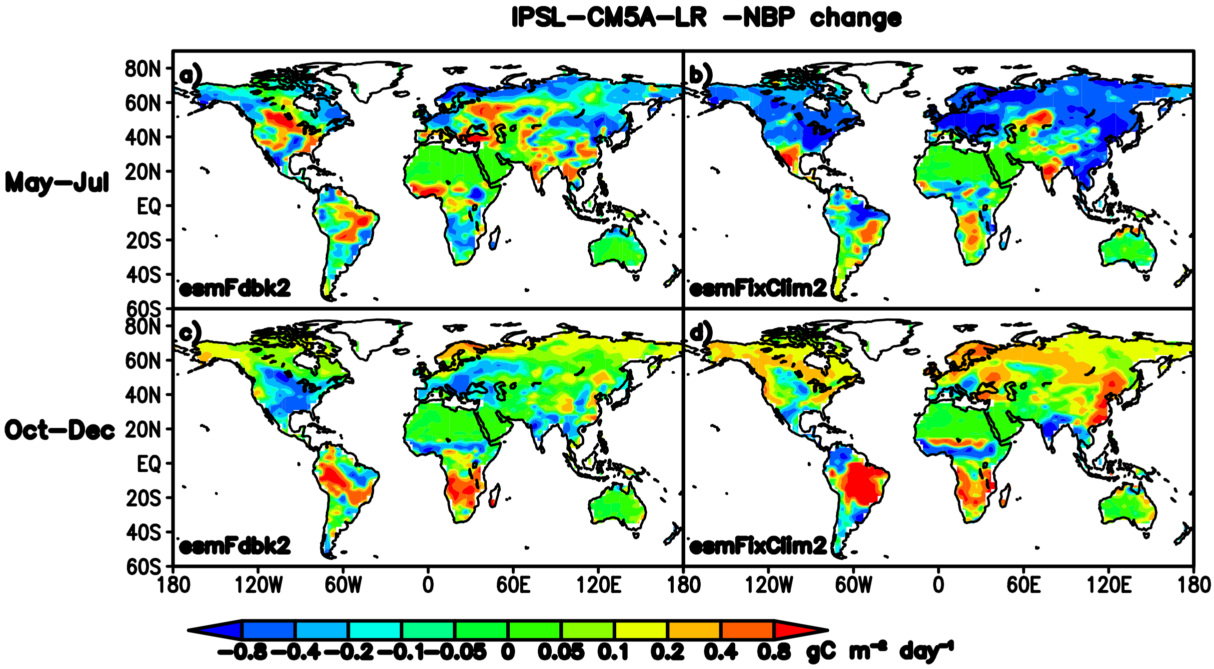

Figure 7. Same as figure 6, but for IPSL-CM5A-LR. Both the carbon uptake in peak growing season and net carbon release in dormant season are clearly dominated by changes in atmospheric CO_2 rather than climate for this model.

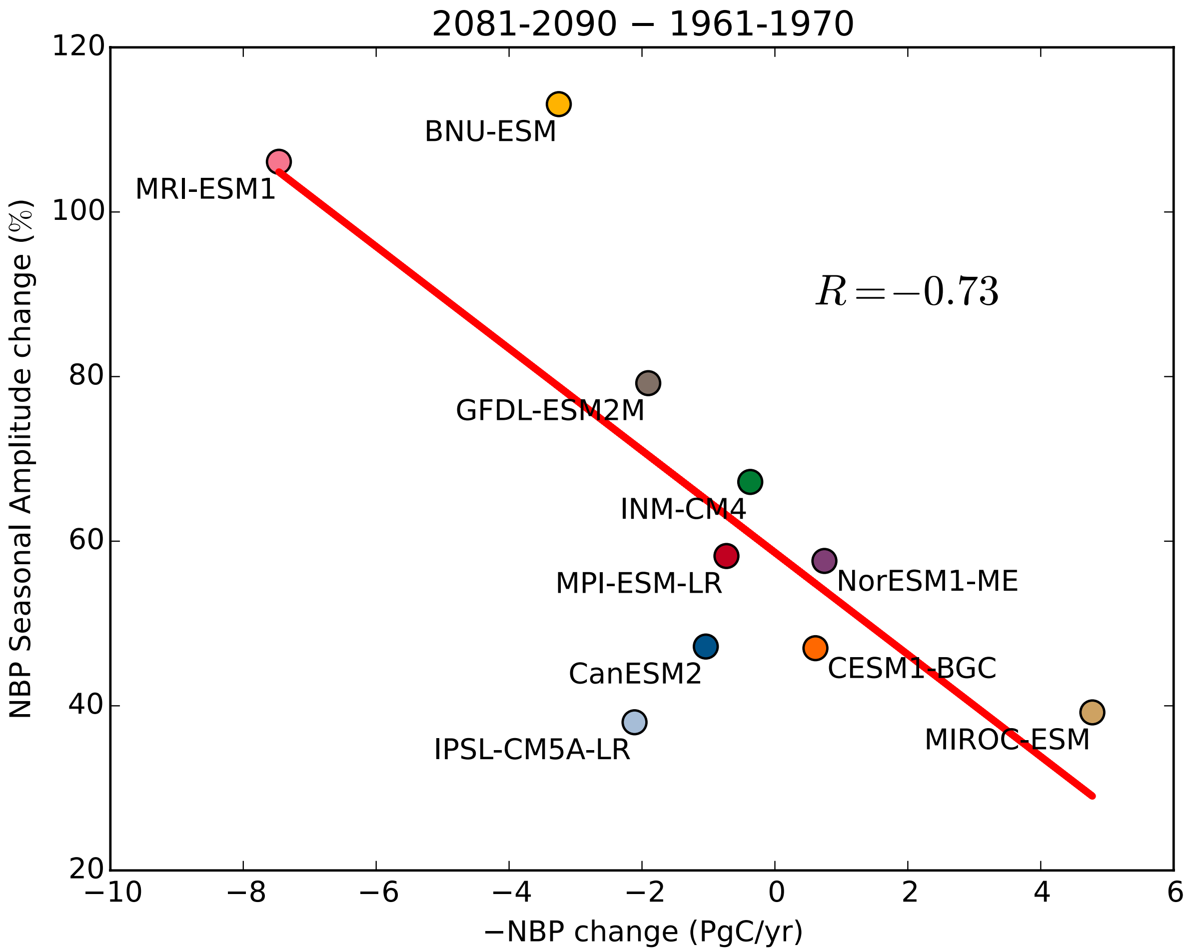

Figure 8. Relationship between −NBP change and change of NBP seasonal amplitude, calculated as the differences between 2081-2090 and 1961-1970 for 10 CMIP5 ESMs. The negative cross-model correlation (R=−0.73, p<0.05) suggests that a model with a larger net carbon sink increase is likely to simulate a larger change in NBP seasonal amplitude.

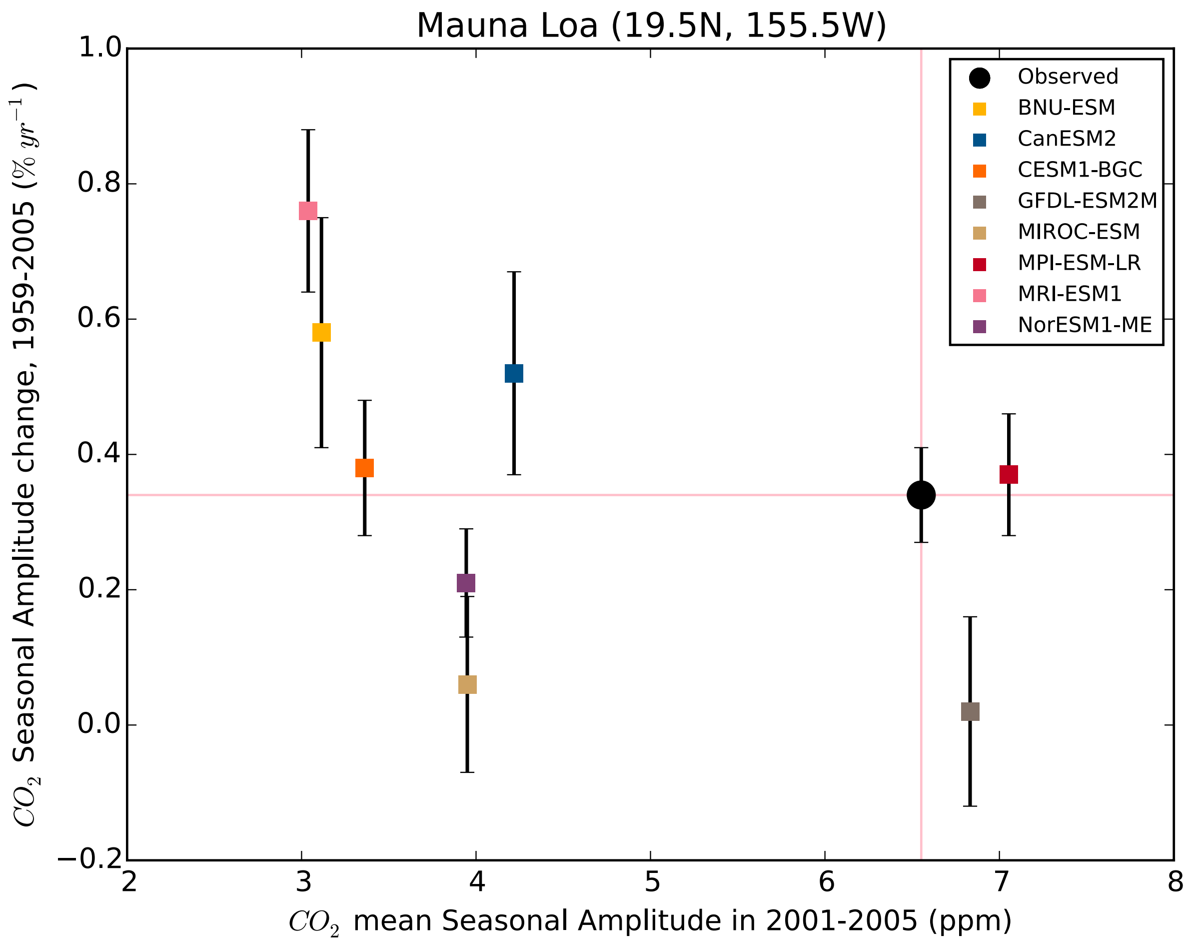

Figure 9. CO_2 mean seasonal amplitude (ppm) during 2001-2005 and changes of CO_2 seasonal amplitude at Mauna Loa during 1959-2005 (% yr^{-1}, linear trend) from eight CMIP5 models and observation. The big black circle represent surface CO_2 observation at Mauna Loa, Hawaii (19.5°N, 155.6°W; 3400m above sea level). The colored squares represent the 700 hPa (close to the altitude of Mauna Loa station surface) CO_2 output at the original grid that covers Mauna Loa from each of the eight models. Error bars indicate ±1 standard error in the trend calculation. Compared to the surface observation, only MPI-ESM-LR and GFDL-ESM2M overestimate CO_2 mean seasonal amplitude at Mauna Loa, while the other models underestimate this amplitude. Models split between overestimating and underestimating the CO_2 seasonal amplitude change at Mauna Loa.

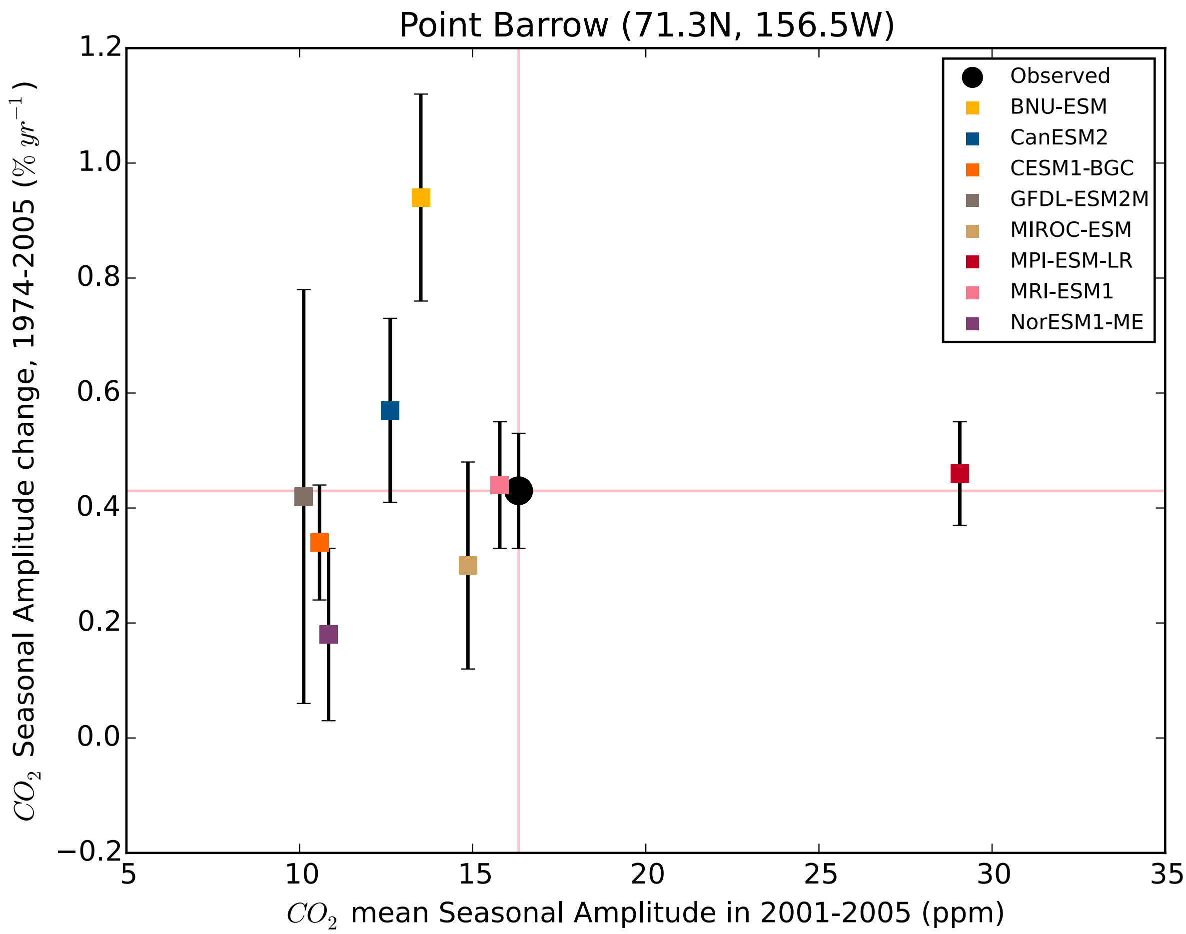

Figure 10. CO_2 mean seasonal amplitude (ppm) during 2001-2005 and change of CO_2 seasonal amplitude at Pt. Barrow during 1974-2005 (% yr^{-1}, linear trend) from eight CMIP5 ESMs and observation. The big black circle represent surface CO_2 observation at Point Barrow, Alaska (71.3°N, 156.5°W; 11m above sea level). The colored squares represent the CO_2 output at lowest model level (four models at 1000 hPa, and four at 925 hPa) at the original grid that covers Point Barrow from each of the eight models. Error bars indicate ±1 standard error in the trend calculation. Compared to the surface observation, only MPI-ESM-LR overestimate the CO_2 mean seasonal amplitude at Point Barrow, while the other models underestimate this amplitude. Models split between overestimating and underestimating the CO_2 seasonal amplitude change at Point Barrow.

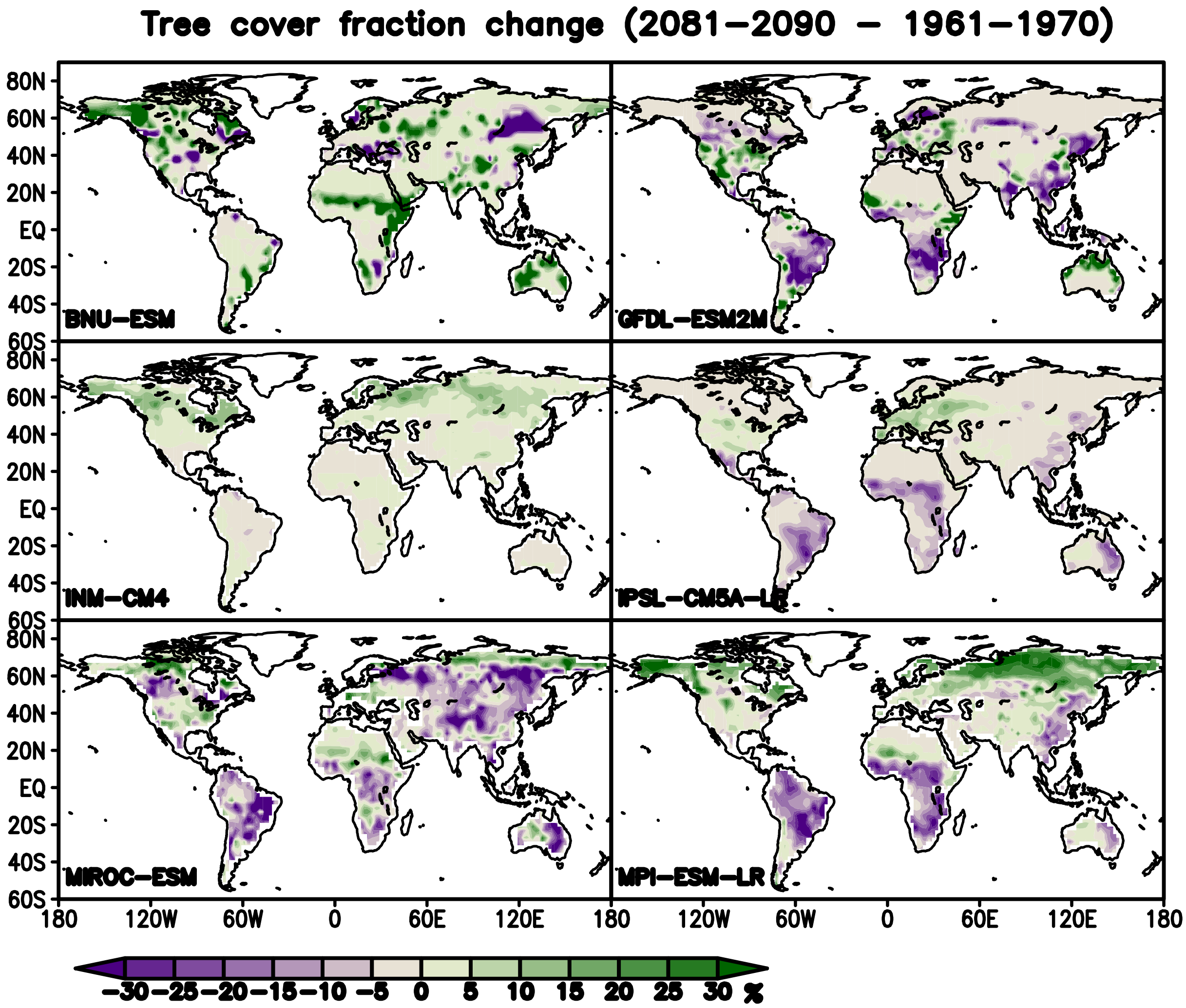

Figure 11. Changes of tree cover fractions between future (2081-2090) and historical (1961-1970) periods from six CMIP5 ESMs. The values represent fractional cover changes in each grid cell, instead of relative change of tree cover. For MPI-ESM-LR and INM-CM4, tree fraction has increased over wide areas of the Northern high latitude regions. For MIROC-ESM, tree fraction has generally decreased over the same regions, possibly in response to a hotter and drier climate condition.

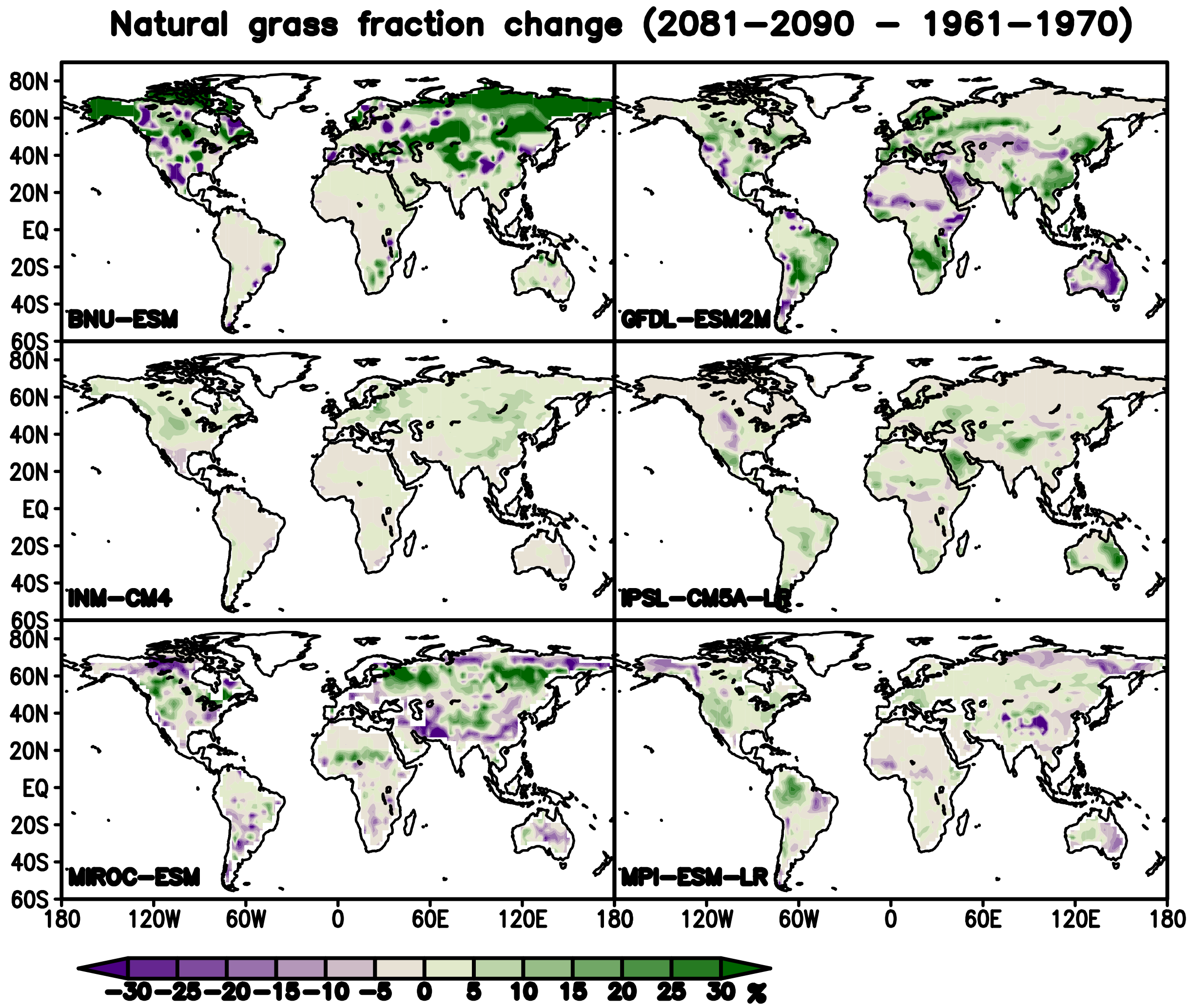

Figure 12. Changes of natural grass fractions between future (2081-2090) and historical (1961-1970) periods from six CMIP5 ESMs. The values represent fractional cover changes in each grid cell, instead of relative change of natural grass cover. Notable increase over the Northern high latitude regions is found for BNU-ESM.